Mapping Fluorophore Distributions in Three Dimensions by Quantitative Multiple Angle-Total Internal Reflection Fluorescence Microscopy

Bence P. Ölveczky, N. Periasamy, and A. S. Verkman

Departments of Medicine and Physiology, Cardiovascular Research Institute, University of California, San Francisco, California 94143 USA

ABSTRACT   The decay of evanescent field intensity beyond a dielectric interface depends upon beam incident angle, enabling the 3-d distribution of fluorophores to be deduced from total internal reflection fluorescence microscopy (TIRFM) images obtained at multiple incident angles. Instrumentation was constructed for computer-automated multiple angle-TIRFM (MA-TIRFM) using a right angle F2 glass prism (n_r 1.632) to create the dielectric interface. A laser beam (488 nm) was attenuated by an acoustooptic modulator and directed onto a specified spot on the prism surface. Beam incident angle was set using three microstepper motors controlling two rotatable mirrors and a rotatable optical flat. TIRFM images were acquired by a cooled CCD camera in ~0.5 degree steps for >15 incident angles starting from the critical angle. For cell studies, cells were grown directly on the glass prisms (without refractive index-matching fluid) and positioned in the optical path. Images of the samples were acquired at multiple angles, and corrected for angle-dependent evanescent field intensity using "reference" images acquired with a fluorophore solution replacing the sample. A theory was developed to compute fluorophore z-distribution by inverse Laplace transform of angle-resolved intensity functions. The theory included analysis of multiple layers of different refractive index for cell studies, and the anisotropic emission from fluorophores near a dielectric interface. Instrument performance was validated by mapping the thickness of a film of dihexyloxacarbocyanine in DMSO/water (n_r 1.463) between the F2 glass prism and a plano-convex silica lens (458 mm radius, n_r 1.463); the MA-TIRFM map accurately reproduced the lens spherical surface. MA-TIRFM was used to compare with nanometer z-resolution the geometry of cell-substrate contact for BCECF-labeled 3T3 fibroblasts versus MDCK epithelial cells. These studies establish MA-TIRFM for measurement of submicroscopic distances between fluorescent probes and cell membranes.

INTRODUCTION

Total internal reflection (TIR) is used extensively in fiberoptics and biosensors. Light incident on a dielectric interface (from a higher to a lower refractive index medium) at a supercritical angle (defined by Snell's law) is totally reflected back into the higher refractive index medium. An exponentially decaying evanescent field is created in the lower refractive index medium. The exponential decay constant of the evanescent field intensity is typically 25–400 nm and depends on media refractive indices, laser illumination angle, and wavelength. Energy can be deposited in the evanescent field if absorbing chromophores are present. The absorbed energy can be dissipated nonradiatively, or if the chromophore has non-zero quantum yield, by fluorescence emission.

The ability to excite fluorescent probes very near a dielectric interface has been exploited in several biological applications. Binding affinities of soluble fluorescent ligands to surface-immobilized receptors are readily measured by steady-state TIR fluorescence intensities (Thompson et al., 1997). Ligand binding rates are measured from the recovery of TIR fluorescence after irreversible photo-

bleaching of bound ligands (Stout and Axelrod, 1994; Hsieh and Thompson, 1994; 1995). TIR fluorescence has also been used to qualitatively map the surface topography of cell-substrate contacts by the selective excitation of cell-associated fluorophores near a transparent substrate support (Axelrod, 1981; Axelrod et al., 1984; Lanni et al., 1985; Gingell et al., 1985; Reichert and Truskey, 1990). Our laboratory has utilized TIR fluorescence to measure relative cell volume from the dilution of soluble fluorescent probes in the cytoplasm (Farinas et al., 1995), and to quantify the viscosity of cell cytoplasm near the plasma membrane by measurement of time-resolved anisotropy (Bicknese et al., 1993) and photobleaching recovery (Swaminathan et al., 1996) of aqueous-phase fluorophores.

It has been recognized for many years that the dependence of the decay of evanescent field intensity on laser illumination angle can provide quantitative information about distances between fluorophores and a dielectric interface (Reichert et al., 1987; Hellen and Axelrod, 1987; Rondalez et al., 1987; Suci and Reichert, 1988; Burmeister et al., 1994). As described in the Theory section, the z-axis distribution of fluorophores can be recovered by inverse Laplace transform of fluorescence intensities measured at multiple laser illumination angles. Fluorescence image acquisition can thus provide information about fluorophore z-distribution with a resolution of tens of nanometers, and x,y-distance information with resolution of under one micron. Multiple-angle TIR has the potential to measure submicroscopic distances in living cells that cannot be mea-

sured by existing techniques. Possible applications include quantitative 3-d mapping of cell-substrate contact geometry, measurement of submicroscopic distances between cell membranes and the underlying spectrin and actin skeletons, and kinetic analysis of vesicular endo and exocytosis events.

The purpose of this study was to develop and evaluate the theory, instrumentation, and practical experimental strategies to apply *Multiple Angle-Total Internal Reflection Fluorescence Microscopy* (MA-TIRFM) for measurement of submicroscopic distances in living cells. Instrumentation was constructed to direct a narrow laser beam onto a cell sample at a series of precise angles and to collect high-magnification fluorescence images. The theory and image analysis routines were developed to compute 3-d fluorophore distribution maps from the image sets. The method was validated using a known fluorophore distribution, and applied to quantify cell-substrate contact geometry in fibroblasts and epithelial cells.

THEORY

Distance determination by MA-TIRFM

The evanescent field established by TIR illumination at a dielectric interface penetrates into the medium of lower refractive index and excites fluorophores near the interface. The evanescent field intensity, $I(z)$, decays exponentially with distance z from the interface:

$$I(z) = I(0) \exp(-z/d) \tag{1}$$

where $I(0)$ is the intensity at the interface. The exponential depth decay constant, d, is:

$$d = (\lambda/4\pi)(n_1^2 \sin^2\theta - n_2^2)^{-1/2} \tag{2}$$

where n_1 and n_2 are the refractive indices of the high and low refractive index media, respectively; λ is the wavelength of incident light in vacuum, and θ is the incident angle. $I(0)$ depends on incident angle and polarization of the incident light. For s-polarized light (used in our experiments), $I(0) = |A_s|^2 \cos^2\theta/(1 - n_2^2/n_1^2)$ (Axelrod et al., 1984), where A_s depends on beam intensity.

The strategy to measure 3-d fluorophore distributions using MA-TIRFM is to exploit the dependence of the decay constant, d, on incident angle θ. If $D_{x,y}(z)$ is the z-distribution of fluorophores (at each x,y position in the sample plane), then the measured fluorescence intensity (at a given x,y pixel in the image), $F_{x,y}(\theta)$, is:

$$F_{x,y}(\theta) = I_{x,y}(0, \theta) \int_0^\infty D_{x,y}(z) \exp[-z/d(\theta)]dz \tag{3}$$

where $I_{x,y}(z = 0, \theta)$ is the intensity of the evanescent field at the interface. It is noted that the expression for $F_{x,y}(\theta)$ formally defines the Laplace transform of $D_{x,y}(z)$. Our strategy is to eliminate the angle-dependent factor $I_{x,y}(0, \theta)$ by measuring the fluorescence, $F_{x,y}^{ref}(\theta)$, of a known fluorophore

distribution for each incident angle. A practical choice for the reference distribution has proven to be a uniformly distributed fluorophore in solution, producing a fluorescence intensity:

$$F_{x,y}^{ref}(\theta) = I_{x,y}(0, \theta)c_{ref} d(\theta) \tag{4}$$

where c_{ref} depends on reference fluorophore concentration, molar absorbance, and quantum efficiency. Quantitative angle-resolved determination of:

$$G_{x,y}(p) = F_{x,y}(\theta) \, d(\theta)/F_{x,y}^{ref}(\theta) \tag{5}$$

where $p = 1/d(\theta)$, thus formally permits the recovery of the $D_{x,y}(z)$ distribution by inverse Laplace transform of $G_{x,y}(p)$.

For the measurements reported in this study, the functional forms of $D_{x,y}(z)$ are known, permitting the angle-resolved intensity distribution $G_{x,y}(p)$ to be fitted directly to an analytic expression for the Laplace transform. In the case of a top-hat function where the uniform fluorophore layer extends from $z = 0$ to $z = h$ [$D_{x,y}(z) = c_{sample}$ for $z < h_{x,y}$ and $D_{x,y}(z) = 0$ for $z > h_{x,y}$, where c_{sample} is related to sample fluorophore concentration, molar absorbance and quantum yield], the analytical expression for the Laplace transform of $D_{x,y}(z)$ is:

$$G_{x,y}(p) = k[(1/p) - (1/p)\exp(-ph_{x,y})] \tag{6}$$

where k is a global constant (identical for all pixels) equal to c_{sample}/c_{ref}. If the same fluorophore at identical concentration is used for sample and reference, then $k = 1$. For a delta function [$D_{x,y} = c_{sample}\delta(z - h_{x,y})$], which would apply to a fluorophore-labeled cell membrane:

$$G_{x,y}(p) = k[\exp(-ph_{x,y})] \tag{7}$$

For a shifted step function [$D_{x,y}(z) = 0$ for $z < h_{x,y}$ and $D_{x,y}(z) = c_{sample}$ for $z > h_{x,y}$], which would apply to uniform staining of cell cytoplasm:

$$G_{x,y}(p) = k(1/p) \exp(-ph_{x,y}) \tag{8}$$

For Eqs. 6–8, the parameters [k and $h_{x,y}$] or $h_{x,y}$ alone, are deduced by nonlinear least-squares regression of experimentally measured $G_{x,y}(p)$ (see below).

The multi-layer problem for measurements in cells

In MA-TIRFM measurements of living cells, the dielectric interface may not be a simple interface between a substrate (e.g., glass prism) and a homogeneous aqueous medium as modeled above. MA-TIRFM measurements on cells thus require consideration of multiple layers—extracellular fluid between the substrate and cell membrane, the membrane, and the cytosol—each having different dielectric properties. The decay of evanescent field intensity is no longer monoexponential. According to Gingell et al. (1987), the expression for $I(z)$ (which replaces Eq. 1) relevant for cell studies

in which fluorophore is dissolved in cytoplasm is:

$$I(z) = 4|A_s|^2 \gamma_1^2 \beta_2^2 \beta_3^2 \exp[-2\beta_4(z - t_2)]/(\gamma_1^2 a_3^2 + \beta_2^2 a_4^2) \quad (9)$$

where $\gamma_1^2 = n_1^2 k_0^2 - k_z^2$, $\beta_2^2 = k_z^2 - n_2^2 k_0^2$; $\beta_3^2 = k_z^2 - n_3^2 k_0^2$, $\beta_4^2 = k_z^2 - n_4^2 k_0^2$, $a_3 = \beta_3(\beta_4 \sinh \beta_2 t_1 + \beta_2 \cosh \beta_2 t_1)\cosh \delta_1 + (\beta_2\beta_4\cosh \beta_2 t_1 + \beta_3^2 \sinh \beta_2 t_1) \sinh \delta_1$, $a_4 = \beta_3(\beta_4 \cosh \beta_2 t_1 + \beta_2 \sinh \beta_2 t_1) \cosh \delta_1 + (\beta_2\beta_4 \sinh \beta_2 t_1 + \beta_3^2 \cosh \beta_2 t_1) \sinh \delta_1$, $\delta_1 = \beta_3(t_2 - t_1)$, $k_0 = 2\pi/\lambda$, and $k_z = n_1 k_0 \sin \theta$. Here, t_1 is the thickness of the extracellular fluid layer (between prism and cell membrane), $t_2 - t_1$ is the membrane thickness, n_1 is the refractive index of the glass prism (1.632), n_2 is the refractive index of the extracellular fluid (1.337), n_3 is the refractive index of the cell membrane (1.44), and n_4 is the refractive index of the cell cytoplasm (1.37). It is assumed that the depth of cytoplasm is much greater than the evanescent field decay depth. This assumption may not be valid at the very periphery of the cell for angles very close to the critical angle. For this reason, only angles of $>1°$ beyond the critical angle were utilized for the cell studies below, generally corresponding to a decay constant of <200 nm.

Due to the difficulty in applying Eq. 9 in the data analysis, our strategy in cell studies was to perform distance computations assuming a uniform cytoplasmic refractive index in the evanescent field. A correction factor (generally under 10% change in computed $h_{x,y}$) was generated based on a simulated comparison of the exact solution to the multi-layer problem (Eq. 9) with the approximate solution for the case of an assumed uniform refractive index (Eq. 1). Validation of the strategy and correction factors for multi-layer geometry are presented in the Results section.

Nonuniformity of fluorescence emission near a dielectric interface

An additional factor complicating the quantitative determination of distances by MA-TIRFM is the nonuniformity of emission from a fluorophore near a dieletric interface. As discussed by Lee et al. (1979), Burghardt and Thompson (1984), and Hellen and Axelrod (1987), the fluorescence collection efficiency depends on fluorophore-interface distance, the geometry of the collection optics (lens numerical aperture), the excitation polarization, and refractive indices.

For emission from fluorophores close to an interface (<500 nm, as is the case for TIR illumination) both far-field and near-field effects must be considered. For a single dielectric interface with the emitting dipole and the point of observation in the lower refractive index medium, the observed emission consists of the propagating light (the far field of the dipole) emitted directly from the dipole and the light reflected off the interface. The radiation pattern due to the near field of the dipole consists of exponentially decaying electric fields that do not propagate in the aqueous medium. Interaction of the decaying near fields with the surface can produce propagating waves in the glass, causing an increase in the power emitted from a dipole with constant

amplitude (a model usually used to describe fluorescence emission) as it becomes closer to the interface. Because the emitted power from a fluorophore in the steady state is only as large as the constant absorbed power (for unity quantum yield), the fluorophore is modeled as a constant power and variable amplitude oscillating dipole. The mathematical and physical basis for this process has been reported (Hellen and Axelrod, 1987) and the relevant considerations to our system are provided in the Appendix. The computations described in the Appendix give the distance-dependent collection efficiency, $Q(z)$, for our collection geometry for random dipole orientation and s-polarized excitation light. Defining $Q(z)$ as the fraction of the total energy dissipated by a fixed power dipole that is collected by a microscope objective, the measured fluorescence at a pixel (x, y) from a fluorophore distribution, $D_{x,y}(z)$, is:

$$F_{x,y}(\theta) = I_{x,y}(0, \theta) \int_0^\infty D_{x,y}(z) \, Q(z) \, \exp[-z/d(\theta)]dz \quad (10)$$

As described above for the multi-layer problem, our strategy to account for nonuniform fluorescence emission is to generate correction factors using the exact theory. The MA-TIRFM analysis above (Eq. 3) assumes that collection efficiency is independent of fluorophore distance from the interface. To generate correction factors, $G_{x,y}(p)$ were computed from Eq. 10 and fitted to the inverse Laplace transform of the appropriate fluorophore profiles (Eqs. 6–8). Correction factors were computed from the ratio of $h_{x,y}$ fitted by this procedure to that determined with an assumed uniform collection efficiency. Correction factors (generally $<10\%$) for nonuniform fluorescence emission are presented in the Results section.

INSTRUMENTATION

MA-TIRFM microscope

The output of a 4W argon-ion laser (Innova 70-4; Coherent, Palo Alto, CA) operating in the single line mode (488 nm) was passed through a software controlled acoustooptic modulator (AOM) (model 305A; Quantum Technology; Lake Mary, FL) and a pinhole (diameter 1 mm) to isolate the first-order beam (Fig. 1). To minimize sample photobleaching, the laser beam (generally ~200 mW) was attenuated 1000-fold by the AOM when not acquiring images. To correct for minor fluctuations and drift in beam intensity (generally $<4\%$ in 1 h), the laser output was measured by deflecting part ($\sim3\%$) of the beam onto a photodiode (PDA50; Thorlabs, Newton, NJ) using a coverglass. Spot illumination (~200 μm width) was obtained by passing the beam through a weak biconvex lens (focal length 400 mm) located 600–700 mm (dependent on illumination angle) proximal to the glass prism. This optical configuration results in a spread of the incident angle that is generally <4 min of arc. A pinhole (diameter 500 μm) was positioned in the optical path to minimize diffraction effects.

FIGURE 1 Schematic of MA-TIRFM instrument. The beam from a continuous-wave argon ion laser was directed onto a spot on the prism surface. Beam incident angle was selected by setting the angles of two rotatable mirrors and a rotatable optical flat. Emitted TIR fluorescence was imaged by a cooled CCD camera. See text for details. *Inset.* Device for culturing mammalian cells on the F2 glass prism. Culture medium containing cells was contained in a cylinder in contact with the prism surface. Tight contact was made using an O-ring and rubber band. The prism was held vertically in a Teflon stand.
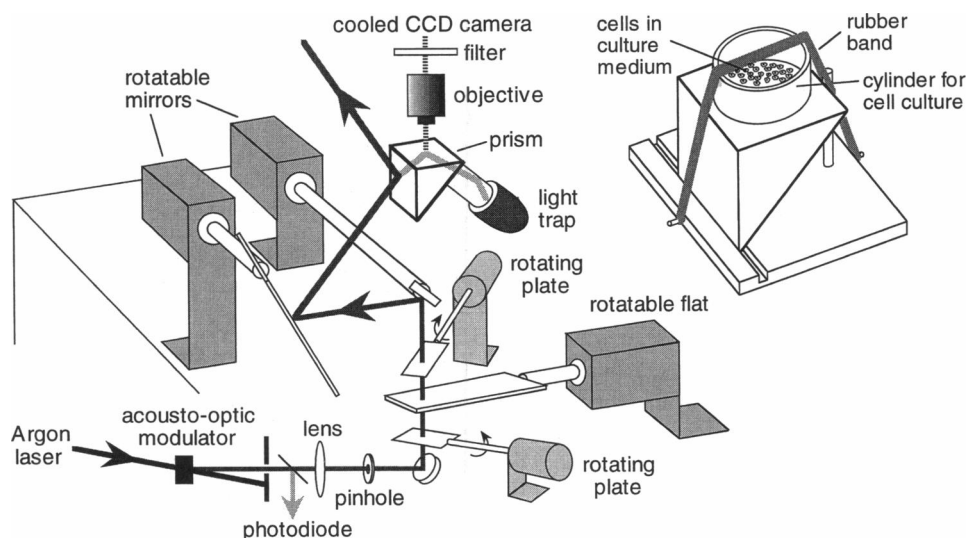
Incident angles for TIR illumination were selected using two rotatable mirrors and an optical flat. The angular orientation of the round mirror (diameter 15 mm, >99% reflectivity at 488 nm, New Focus, CA), the rectangular mirror (20 × 100 mm), and the optical flat (thickness 1 mm) were controlled by three microstepper motors. The motors were driven separately by three 5-phase stepping motor drivers (model UPS502; Nyden Corporation San Jose, CA), and software controlled using a multi-axis motion controller (model MAC-300; Nyden Corporation, San Jose, CA). The angles of the mirrors defined the beam incident angle and direction, and the optical flat controlled out-of-plane beam deviation, compensating for imperfect mirror flatness and axial alignment. In addition, two glass plates (thickness 500 μm) mounted on continuously rotating (300 rpm) motors (model 1219M; Minimotor, Switzerland), with perpendicular axes of rotation, were positioned in the laser beam to improve beam uniformity by averaging speckle and diffraction effects. The beam was directed to the vertical surface of a right angle 2 × 2-cm F2 glass prism (n_r 1.632 at 488 nm, polish 5/10 surface quality; Custom Optical Elements, Las Vegas, NV) held in a prism-holder mounted on a 3-d micromanipulator. The high grade of surface polish was necessary to minimize scattered (non-TIR) light escaping into the sample. The prism was used to create the TIR interface and also functioned as substrate for cells. To prevent secondary reflections of the laser beam inside the prism from transilluminating the sample, a polished F2 glass rod (diameter 2 cm, length 8 cm, Mindrum Precision, Rancho Cucamonga, CA) was coupled to the hypotenuse surface of the prism with a refractive index-matched laser liquid (Liquid code 5763; Cargille Laboratories, NJ) (*light trap*, Fig. 1). A black rubber bag filled with the laser liquid was tied to the distal end of the glass rod to absorb the light. For the calibration (see below), a plano-convex fused silica lens (radius 458 mm) was mounted on a 3-d micromanipulator and positioned above the glass prism to make point contact with the prism near the optical axis of the microscope.

The objective used for the calibration was a 25× long working distance lens (Leitz Wetzlar, Germany; dry, N.A. 0.35) and for the cell experiments a 100× water immersion lens (Leitz; N.A. 1.2). Emitted fluorescence was filtered by a 515-nm long-pass filter (Schott) and imaged by a 512 × 512 pixel, cooled CCD camera (model CH 250; Photometrics, Tuscon, AZ) with a 14-bit analog processor.

To generate specified beam incident angles (generally >15 angles), the angular positions of the two mirrors and the optical flat were established before each set of experiments and stored as a look-up table. The look-up table was accessed for subsequent acquisitions of sample and reference images. Incident angles corresponding to each set of mirror angles were measured from the position of the excitation beam reflection (observed on a strip of white tape on the dark room ceiling) off of the vertical surface of the prism. Incident angles were computed from the location of the reflected spot and Snell's law (to account for refraction in the prism). The prism was positioned in the prism-holder so that the laser beam reflection on the ceiling was insensitive to vertical displacement of the prism, ensuring alignment of the prism surfaces. The optical components were rigidly mounted on a Technical Instruments custom microscope stand positioned on a floating optical table (I-2000 Stabilizer, Newport) in a dark, temperature-controlled and dust-free room.

Software was written in Microsoft C and executed on a Gateway 2000 PC, equipped with analog and digital I/O board (CIO-DAS08-AOH, Computerboards, Mansfield, MA) to measure photodiode signal and set AOM input. The software controlled and coordinated the positioning of the microstepper motors with the photodiode signal, AOM analog output, and image acquisition.

Image analysis

The experimental procedure described below generated images for the reference and sample distributions at each beam

incident angle. In order to exclude "bad" pixels, the images were filtered prior to analysis using a pseudo-median filter with length three as defined by Pratt (1991). The angle-resolved intensity distribution for each pixel, $G_{i,j}(p)$, was obtained from the ratio of sample, $F_{i,j}(\theta)$, and reference, $F_{i,j}^{ref}(\theta)$, images multiplied by the decay constant $d(\theta)$ (Eq. 5). The angle-resolved intensity distribution, $G_{i,j}(p)$, was curve-fitted to an analytic expression for the Laplace transform of the anticipated fluorophore distribution (Eqs. 6–8). Parameter(s) defining the fluorophore distribution were fitted using the Levenberg-Marquardt algorithm (Press et al., 1992). The fitted distance $h_{x,y}$ was corrected for multiple sample refractive index layers (for cell studies) and nonuniform collection efficiency as described in the Theory section. The analysis produced a 3-d map of the fluorophore distribution.

METHODS

Cell culture and fluorophore loading

MDCK-1 cells (ATCC CCL no. 34; American Type Culture Collection, Rockville, MD) and Swiss 3T3 fibroblasts were cultured directly on the F2 glass prisms in DME-H21 medium supplemented with 10% fetal calf serum, 100 U/ml penicillin, and 100 mU/ml streptomycin. Cells were maintained at 37°C in a 95% air:5% CO_2 atmosphere. A prism support for cell culture was constructed in which cells were grown directly onto the prism without the need for refractive index-matched coupling fluid (Fig. 1, inset). A polysulphone cylinder (radius 2 cm, height 1 cm) with an embedded soft O-ring (making contact with the prism) was secured on top of the prism with a rubber band to provide a well for the culture medium. Cells were used 18–20 h after plating and were labeled with 10 μM BCECF-AM (Molecular Probes Inc, Junction City, OR) in PBS. The reference fluorophore (FITC-dextran, Molecular Probes Inc, Junction City, OR) was dissolved in the same solution. After use, prisms were washed serially in ethanol, alkali, and acid, rinsed extensively with distilled water, and stored immersed in ethanol.

Experimental protocol

The prism containing cultured cells was aligned and secured rigidly in the prism-holder by a Teflon screw. The positions of the three microstepper motors for the incident angles were then established as described above. Generally the angles were incremented by ~0.5 degrees, starting from the critical angle. Image acquisition time was set to avoid saturation while maximizing the dynamic range of the pixels. Images of the sample were then acquired in succession at each of the specified laser incident angles. The cells were carefully washed off the prism surface using STV (0.25% Trypsin and 0.2% Versene in saline; UCSF Cell Culture Facility) and water, and were replaced by a uniform film of dissolved fluorescent dye. The excitation beam was attenuated by the AOM for the brighter reference sample. Laser intensity was recorded just before and after each image acquisition and the average was taken to represent the intensity during the exposure. The complete experimental procedure took ~15 min, with ~2 min for multiple-angle image acquisition of the cell sample. A repeat image at the initial angle was recorded after the multi-angle image acquisition to evaluate photobleaching.

Distance calibration using a known fluorophore distribution

To validate the accuracy of distance determination by MA-TIRFM, a known 3-d fluorophore distribution was established by lowering a plano-

convex lens (radius 458 mm) onto a layer of dissolved fluorophore until the curved surface of the lens made point contact with the horizontal surface of the right-angle prism near the center of the field of view (Fig. 2). A fluorescent dye [di-O-C6-(3); Molecular Probes Inc., Junction City, OR] in a DMSO/water mixture was refractive index-matched to the fused silica lens (n_r 1.463 at 488 nm) by immersing the lens in a bath of DMSO while illuminating the prism with the laser beam through the bath. Water was added until the direction of the laser beam exiting the bath was insensitive to movement of the lens. Images were acquired using the 25× dry objective. Reference images were acquired after elevating the lens ~1000 nm above the prism surface.

RESULTS

Theoretical simulations

Predicted angle-resolved intensity functions $G(p)$ (Eq. 5) were computed for three fluorophore profiles, $D(z)$, of significance for biological measurements: delta function (Fig. 3 A), top-hat function (Fig. 3 B), and step function (Fig. 3 C). The simulations showed a strong dependence of absolute $G(p)$ values and the $G(p)$ curve shape on distance parameter h. It is this dependence that is exploited to determine fluorophore-interface distance from fluorescence intensities measured at multiple incident angles.

The influence of experimental noise on the accuracy of parameter recovery from $G(p)$ data was evaluated. Fig. 3 D shows fitted curves to $G(p)$ (for a top-hat function with 14 incident angles) with random noise (average noise-to-signal amplitude 30%) added to each point. Fitted curves are shown for a two-parameter fit (fitting k and h, see Eq. 6), and a one-parameter fit (fitting h only). The recovered values for h were excellent (100 and 97 nm for 1- and 2-parameter fits, respectively). Simulations at different h (25–250 nm) and noise levels (up to 50%) indicated recovery of h values to generally better than 4% accuracy with the 1-parameter fit and 15% accuracy for the 2-parameter fit. Similar results were obtained for simulations using the shifted step function and the delta function. These simulation provide justification for the determination of fluoro-
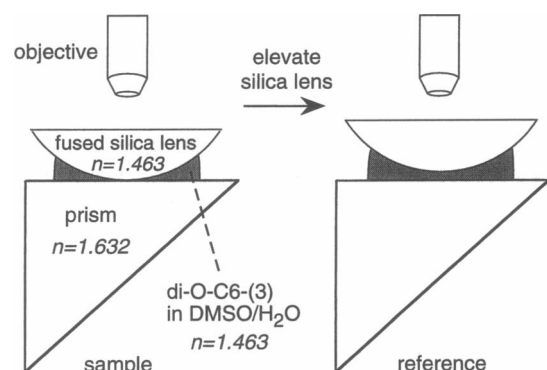

FIGURE 2 Evaluation of MA-TIRFM instrument performance using a known fluorophore distribution. A spherical film of di-O-C6-(3) in DMSO/water was created by making point contact between a fused silica plano-convex lens and the F2 glass prism (left). A uniform "reference" fluorophore distribution was created by raising the silica lens by ~1 μm (right).
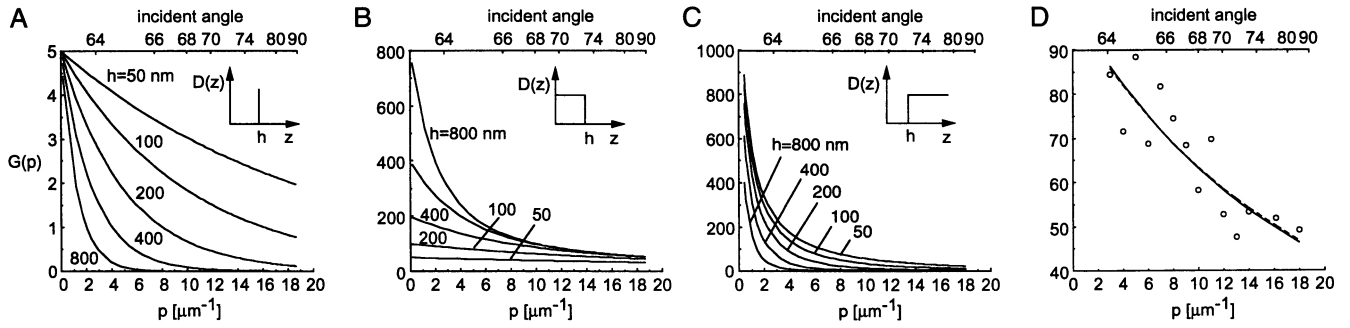
FIGURE 3   Predicted $G(p)$ curve shapes and theoretical accuracy of parameter recovery. $(A–C)$ Angle resolved intensity distributions, $G(p)$, for indicated fluorophore profiles. (A) Delta function, $D(z) = c\delta(z - h)$. (B) Top-hat function, $D(z) = c$ for $0 < z < h$ and 0 for $z > h$. (C) Step function, $D(z) = 0$ for $z < h$ and c for $z > h$. Parameters for $(A–C)$: $n_1 = 1.632$, $n_2 = 1.463$, $\lambda = 488$ nm. (D) Recovery of parameter h from simulated experimental data containing random noise. $G(p)$ values were simulated at 14 incident angles for a top-hat function with $h = 100$ nm. Random noise (30%) was added to each point. $G(p)$ vs. p data were fitted to the inverse Laplace transform of a top-hat function (Eq. 6). Fitted curves for a 1-parameter fit $(dashed\ curve,\ h = 100$ nm) and 2-parameter fit $(solid\ curve,\ h = 97)$ are shown.

phore-interface distances from experimentally derived $G(p)$ ratios.

The recovery of distances in the presence of multiple layers of different refractive indices in the evanescent field (as in cell experiments) was evaluated. $G(p)$ was computed from Eqs. 5 and 9 for a multi-layer configuration consisting of an F2 glass prism (n_r 1.632), a layer of aqueous buffer (n_r 1.337) of variable thickness, a 4-nm thick membrane (n_r

1.44), and cytoplasm containing fluorophore (n_r 1.37). The predicted $G(p)$ $(circles$ in Fig. 4 $A)$ were fitted to the inverse Laplace transform of a top-hat function (as in Fig. 3 $D)$ assuming a uniform refractive index of 1.37. The $G(p)$ data were very well fitted even though the refractive index in the evanescent field is not uniform in this multi-layer simulation. Fig. 4 B shows a correction plot of actual versus recovered h for a shifted step function distribution. Maxi-
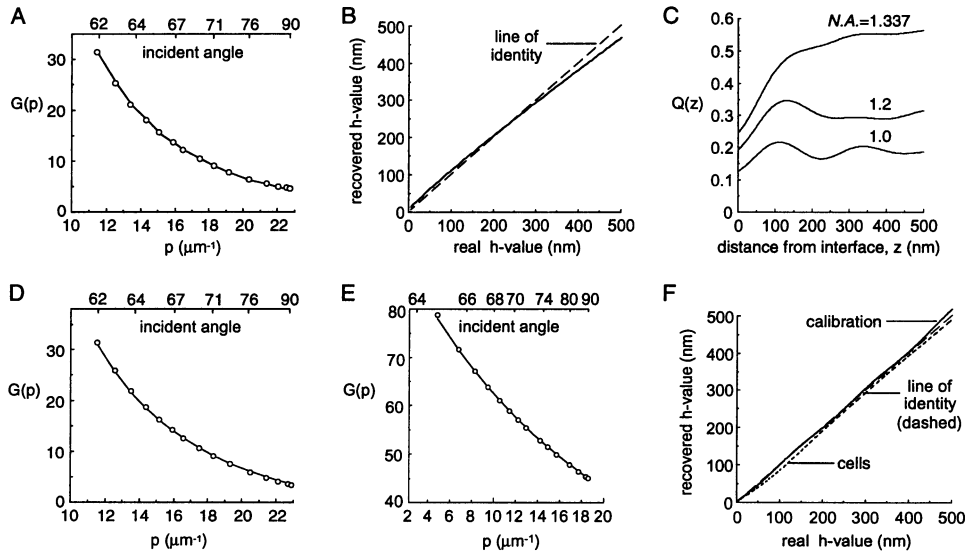

FIGURE 4   Predicted influence on parameter recovery in the presence of multiple refractile layers in the evanescent field, and anisotropic fluorescence emission close to an interface. (A) Simulated $G(p)$ for multi-layer geometry using Eq. 9 for a 96-nm aqueous layer (n_r 1.337), 4-nm cell plasma membrane (n_r 1.44), and cytoplasm containing fluorophore (n_r 1.37). Simulations were done for a shifted step function. Fitted curve shown for an assumed uniform cytoplasmic refractive index of 1.37. See text for details. (B) Correction plot of calculated versus actual h generated for simulations as in (A). (C) Dependence of collection efficiency, $Q(z)$, on distance, z, between fluorophore and dielectric interface computed from equations in the Appendix for varying N.A. with $n_{aq} = 1.337$. $(D$ and $E)$ Simulated $G(p)$ accounting for the distance-dependent collection efficiency, $Q(z)$. (D) Shifted step-function $(h = 100$ nm) with the observation angle corresponding to the optical configuration for cell experiments: N.A. $= 1.2$, $n_{aq} = 1.337$. Evanescent wave intensity calculated using uniform sample refractive index of 1.37. Fitted curve corresponds to $h = 85$ nm. (E) Top-hat function $(h = 100$ nm) with the observation angle corresponding to the calibration experiment: N.A. $= 0.35$, $n_{aq} = 1.3$. The effective aqueous refractive index was calculated based on the precise geometry of the calibration experiment taking into account the refractive index of both the sample ($n_s = 1.463$) and the air between the lens and the objective. Evanescent wave intensity calculated using sample refractive index of 1.463. Fitted curve corresponds to $h = 98$ nm. (F) Correction plot of calculated versus actual h generated for simulations as in (D) and (E). Simulations were done for an excitation wavelength of 488 nm, emission wavelength of 510 nm, and prism refractive index of 1.632.

mum deviation from the true h value was <15 nm for $h <$ 400 nm. Deviations were <5 nm when the refractive index of the aqueous medium was increased from 1.337 to 1.36 (for example, by addition of 46% dextran). Similar results were obtained in correction plots for the delta and top-hat functions. These computations indicate that $G(p)$ curve shape analysis cannot resolve single- versus multi-layer geometry, and that the distance correction can be minimized by increasing the refractive index of the aqueous layer. The plot in Fig. 4 B will be used below to generate correction factors to correct the apparent distances determined in the cell experiments.

The dependence of fluorescence emission collection efficiency, $Q(z)$, on fluorophore-interface distance was evaluated for different collection geometries (different numerical apertures, N.A.). Computations were done as described in Eq. 10 and the Appendix using glass and aqueous media refractive indices of 1.632 and 1.337, respectively, and 510-nm wavelength for fluorescence emission (excitation wavelength 488 nm) (Fig. 4 C). The curve for N.A. = 1.337 represents the collection of all light emitted into the aqueous media. As predicted by the theory, the collection efficiency is lower for fluorophores closer to the surface. Beyond 100 nm, the sensitivity of the collection efficiency to fluorophore-interface distance decreases substantially.

Angle-resolved intensity functions, $G(p)$, were calculated from Eqs. 5 and 10 for the optical geometries used in the experiments below. The parameters were chosen to correspond to the calibration experiment (N.A. = 0.35, n_{aq} = 1.463, n_{glass} = 1.632) and the cell studies (N.A. = 1.2, n_{aq} = 1.337, n_{cell} = 1.37, n_{glass} = 1.632). Computed $G(p)$ were fitted to the inverse Laplace transform of a top-hat function (for calibration study, Fig. 4 D) and a shifted step function (for cell studies, Fig. 4 E). It is noted that the distance-dependent collection efficiency has little effect on $G(p)$ curve shape, indicating that effects of nonuniform collection efficiency, even if substantial, can be compensated for in a quantitative manner. As was done above for the multi-layer problem, the small error in recovered h values is corrected using plots in Fig. 4 F. For the case of the top-hat function (with parameters as in the calibration experiment) the deviations from the line of identity are minor (<5 nm), and become very small beyond h = 100 nm (<2% deviation). For the shifted step function the deviations are slightly larger, but generally under 15 nm.

Instrument performance

Instrument performance was evaluated by imaging a known fluorophore distribution that was established by lowering the curved surface of a plano-convex lens onto a layer of fluorophore-containing solution on the prism surface (see Fig. 2 and description in Methods). Sample and reference images were obtained at 22 incident angles from 64 to 77 degrees. Representative images for three incident angles are shown in Fig. 5 A. Image intensities were strongly depen-
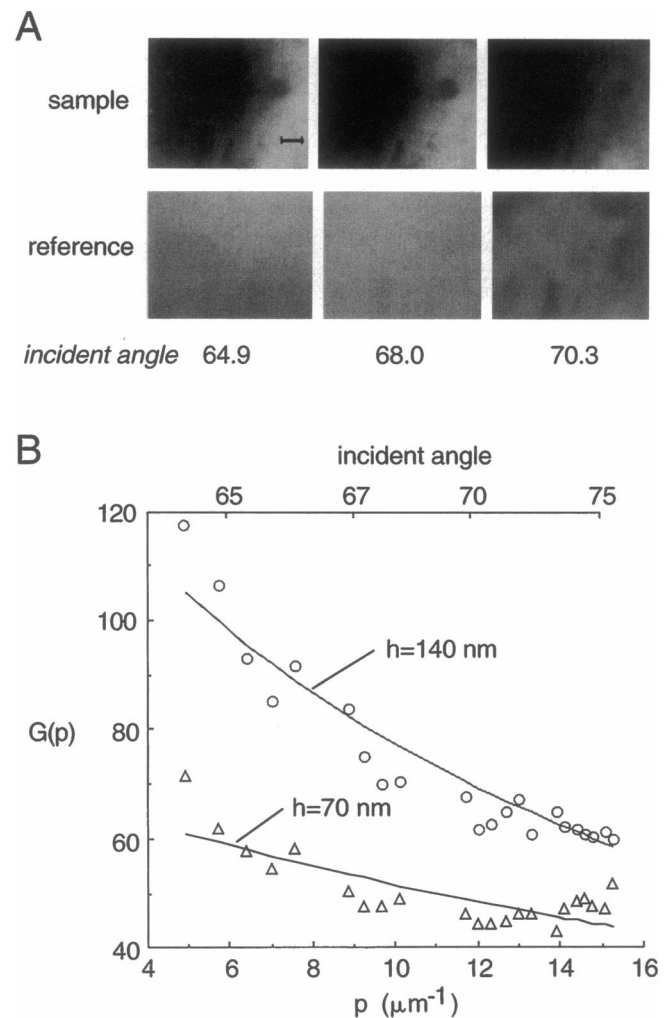

FIGURE 5   Evaluation of MA-TIRFM instrument performance using a curved film of fluorescent solution. The solution film was created as shown in Fig. 2 and described in the text. (A). Fluorescence intensity images of the sample (silica lens in contact with prism, top) and reference (silica lens raised above prism, $bottom$). Representative images shown for 3 of 22 incident angles. Bar, 5 μm. (B) Nonlinear regression of angle-resolved intensity distributions shown for two randomly chosen pixels (of 64,000 pixels). Data were fitted to a top-hat function (Eq. 6) with fitted h values as shown.

dent on incident angle, and the sample images showed intensity variations in the image plane due to the nonuniform film thickness. Experimentally deduced angle-resolved intensity distributions, $G(p)$, were fitted to the inverse Laplace transform of a top-hat function (Eq. 6) in accordance with the expected fluorophore profile. Fig. 5 B shows the fit to $G(p)$ for 2 pixels in the image giving indicated fitted h values. $G(p)$ for each pixel were individually fitted to give h values for each x,y point in the image. A small correction for nonuniform collection optics was then made as per Fig. 4 F.

A 3-d map of solution layer z-thickness as a function of x,y-position in the plane is shown as a 3-d contour plot in Fig. 6 A. The predicted lens shape, computed by radial
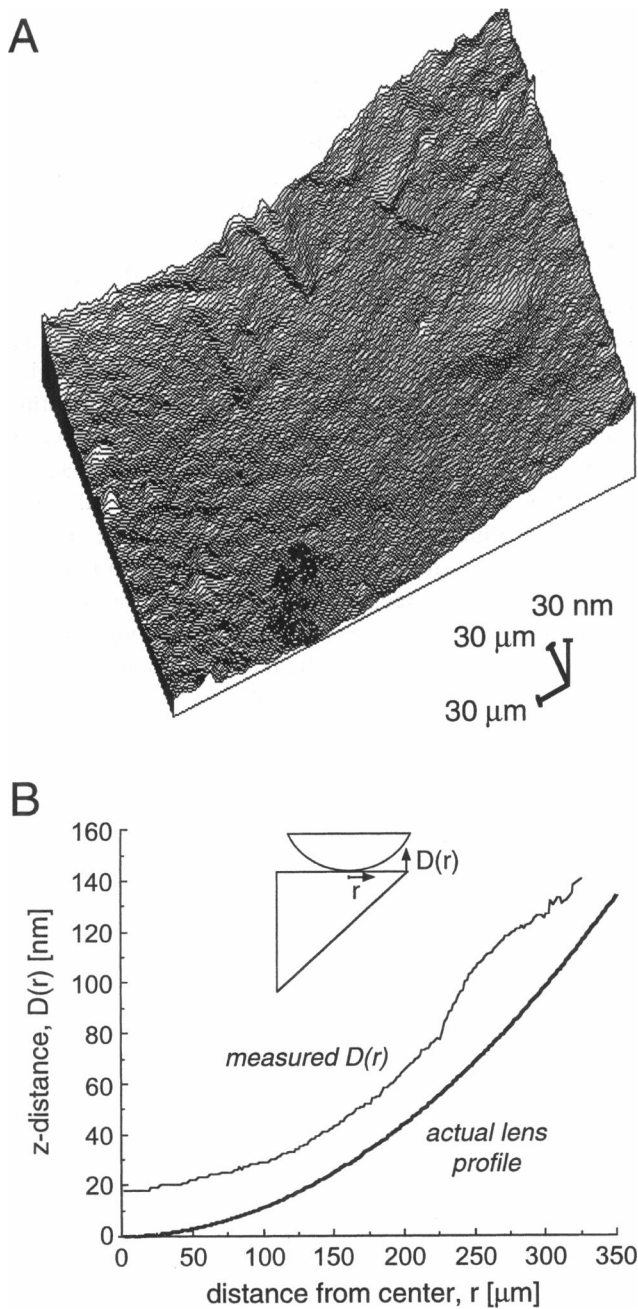
A

30 nm
30 μm
30 μm

B

FIGURE 6   3-d distribution of solution thickness from data set shown in Fig. 4. (*A*) 3-d contour plot reconstruction of the fluid layer between the flat prism (*bottom*) and curved surface of plano-convex lens (*top*). (*B*) Solution thickness as a function of distance from lens-prism contact point, $D(r)$, determined by radial averaging of data from (*A*). Actual lens profile determined from manufacturers specification of 458 nm lens radius.

averaging of the 3-d distribution (Fig. 6 *B*), was in very good agreement with the known lens profile (458 nm radius of curvature). The non-zero predicted z-distance at the center of the distribution was a consistent finding, and might be related to unavoidable adsorption of the fluorophore to the prism surface and/or to imperfect lens-prism contact. The choice of a cyanine fluorophore and DMSO/water solvent was made after testing a series of fluorophore/solvent com-

binations (e.g., FITC-dextran, glycerol/water) for minimal surface adsorption. Additional precautions included extensive cleaning of the prism and lens surfaces before use, and rapid data acquisition after applying the fluid layer.

Measurement of cell-substrate contact geometry

The topology of cell-substrate contact was measured for Swiss 3T3 fibroblasts and MDCK epithelial cells stained with BCECF. Images were acquired at 17 incident angles. Computations were performed using a sample refractive index of 1.37, correcting for the multi-layer refractive index distribution using the plot in Fig. 4 *B*. Fig. 7 shows fluorescence intensity images of a 3T3 fibroblast (*top*) and MDCK cell (*bottom*) for three incident angles. Image intensities depended strongly on incident angle. The regions of closest cell contact with the substrate are preferentially illuminated as the evanescent field penetration depth decreases with increased incident angle. Cell images were quite nonuniform for the 3T3 fibroblasts, indicating widespread presence of close contacts (as defined by Izzard and Lochner, 1976).

The angle resolved intensity distributions, $G(p)$, were fitted to the inverse Laplace transform of a shifted step function (Eq. 8), assuming uniform staining of cytoplasm. Since different fluorophores were used in the sample and reference acquisitions, k was taken as a fitted global parameter that is the same for all pixels. Fig. 8 *A* shows the deduced 3-d cell contours at the cell-substrate interface and Fig. 8 *B* shows a gray-scale contact map. Representative 1-d plots of contact geometry along dashed lines in Fig. 8 *B* are shown in Fig. 8 *C*. The data for 3T3 fibroblasts indicate the close contact regions to be between 20 and 45 nm from the surface. These results are in very good agreement with previous studies on fibroblasts using electron microscopy and interference reflection microscopy (Abercrombie et al.,
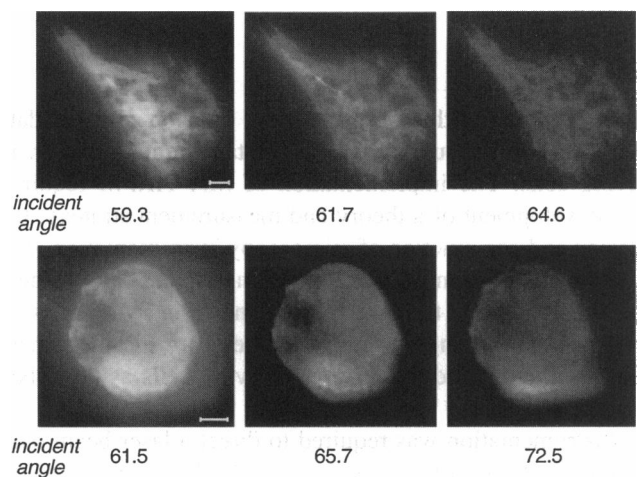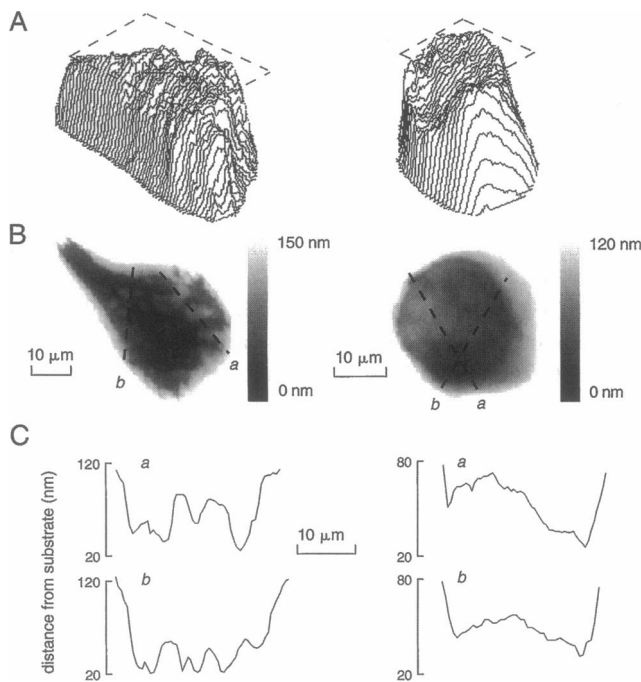

incident angle   59.3   61.7   64.6

incident angle   61.5   65.7   72.5

FIGURE 7   Fluorescence intensity images of a Swiss 3T3 fibroblast (*top*) and MDCK cell (*bottom*) at indicated laser incident angles. Cells were cultured directly on the F2 glass prism, cytoplasm was stained with BCECF, and cell were imaged as described in Methods. Bar = 5 μm.

FIGURE 8 Cell-substrate contact geometry of 3T3 fibroblast (*left*) and MDCK cell (*right*). (*A*) 3-d contour plots showing cell-substrate contact geometry (*facing up*). The approximate location of the prism surface is shown (*dashed box*). (*B*) Gray-scale map of cell-substrate contact geometry. (*C*) Representative cross sections [*dashed lines* in (*B*)] from the contact map showing absolute cell-substrate distances.

1971; Heaysman and Pegrum, 1973; Chen and Singer, 1982; Burridge et al., 1988). The plots in Fig. 8 *B* (*left*) show the contact regions to be separated by 5–10 μm. Similar results were reported for analysis of contacts in bovine endothelial cells (Truskey et al., 1992). Interestingly, the cell-substrate contact geometry was found to be somewhat different for MDCK cells (Fig. 8, *right*), where the close contacts are located mainly at the periphery of the cell.

DISCUSSION

The purpose of this study was to develop and validate MA-TIRFM for submicroscopic distance determination in living cells. The implementation of MA-TIRFM required the development of a theory and measurement strategy, the design and construction of microscopy instrumentation, validation on a system with known geometry, and development of a methodology to make measurements in living cells. A number of challenges were encountered in the instrument design, theory, and application to living cells as described below.

Instrumentation was required to direct a laser beam onto a specified spot on a sample at multiple incident angles. Additional instrumentation requirements for quantitative measurements included minimal angular spread in the incident beam, minimal scattering by the prism surface, minimal secondary reflections, and fairly uniform beam profile.

Our strategy to specify beam direction was to use two rotatable mirrors and a rotatable optical flat as shown in Fig. 1. High precision and reproducibility were obtained using microstepper motors to position the three rotatable components. The planar optics of this system gave an incident beam with minimal angular spread and permitted effective elimination of secondary reflections by a light trap. An alternative optical configuration, consisting of a single rotatable mirror, off-axis elliptical reflector, and hemicylindrical sapphire prism, was initially tested but found to be inadequate because of alignment difficulties, beam angular spread, and secondary reflections. A right-angle F2 glass prism was selected because of its clarity, minimal autofluorescence and phosphorescence, high enough refractive index to permit a wide range of subcritical incident angles, and a low enough refractive index to permit full range multi-angle illumination with only two rotatable mirrors. High surface polish was found to be essential to minimize surface scattering effects. With 5/10 polish, no scattered light was detected when viewing the emission of fluorophores beyond the evanescent field (with a fluorescent layer positioned at 200 μm from the interface). The prism surface itself was used to create the dielectric interface for solution and cell studies. Based on pilot experiments, it was concluded that the use of coverglasses and refractive index-matching coupling fluids would present considerable difficulties in terms of precise specification of sample geometry, and imperfect optical properties of the coupling fluid. A device was constructed to culture mammalian cells on the top surface of the prism without disturbing the remaining optical surfaces.

An essential component of the method was the correction of sample images for angle-dependent beam intensity profiles at the prism surface. Since beam intensity profiles cannot be predicted accurately, correction was carried out by recording reference images of a known fluorophore distribution at each incident angle. An important consideration in cell studies was to account theoretically for the multilayer geometry that consists of an extracellular aqueous space, lipid cell membrane, and cytoplasmic interior, each with different thicknesses and refractive indices. Our strategy for the multilayer geometry was to solve the exact multilayer problem using the theory of Gingell et al. (1987), and to generate correction factors to correct the distance parameter deduced from data regression to single-layer geometry. Fortunately, the fits to $G(p)$ for single-layer geometry were excellent and the correction factors were near unity. As demonstrated by the simulations, an alternative experimental strategy to minimize effects of multilayer geometry would be the addition of macromolecular solute (e.g., dextrans, metrizimide) to raise extracellular refractive index to approximate intracellular refractive index. This approach was not used for the measurements of cell contact geometry here to avoid possible effects resulting from the high concentrations of macromolecular solutes needed to increase solution refractive index. An additional theoretical

challenge was to account for the nonuniform fluorescence emission of fluorophores near a dielectric interface. The theory relating collected signal intensity to fluorophore distance distributions (Hellen and Axelrod, 1987) required specification of collection optics, excitation light polarization, fluorophore orientation, and media dielectric properties. Numerical computations indicated that the effect of nonuniform fluorescence emission is predictable and can be accounted for quantitatively by using a correction factor.

There are a number of practical concerns that may limit the resolution of distances by MA-TIRFM. Small imperfections (scratches and digs) at the prism surface disturb the optics, resulting in scattering and local nonuniform illumination. Although very costly and requiring elaborate cleaning procedures, higher degrees of surface polish can be accomplished, as is done for high-power laser optics. Light scattering by intracellular structures might present a limitation to the ultimate resolution of MA-TIRFM. Cellular light scattering was not formally evaluated in this initial study; measurements will be needed comparing different wavelengths (to change scattering) and/or solutions containing membrane permeable solutes (D_2O or glycerol) of different refractive indices. Because of the substantial illumination required for multi-angle image acquisition, photobleaching is a concern for measurements on spatially fixed (nondiffusible) fluorophores. It will be important in measurements on immobile fluorophores to select relatively photostable fluorophores.

Previous work on multiple-angle TIRF has been concerned with mapping the z-dependent concentration profile of artificial polymers (Rondalez et al., 1987) and layers of fluorescein-labeled immunoglobulin (Reichert et al., 1987) adsorbed to glass. The general approach has been tested by reproducing the concentration profiles of Langmuir-Blodgett films (Suci and Reichert, 1988). Quantitative cell studies using TIRF were first conducted by Lanni et al. (1985), where two-angle image acquisition was used to estimate cell-substrate separation distances. Burmeister et al. (1994) refined the technique using multiple angles. There are a number of important differences between those studies and the work reported here. In addition to differences in instrumentation and cell culture/labeling, the present study utilizes the Laplace transform relationship between fluorophore distribution and its normalized angle-resolved intensity function to provide a general method of determining fluorophore distributions, where earlier work was limited to recovering a single well-specified distribution. Previous studies normalized for changing illumination conditions by referencing the measured fluorescence to the fluorescence intensity obtained at a specified incident angle. This normalization requires perfect optical alignment, ideal beam profiles, and does not take into account the nonuniformity of laser beam profile at the interface at different incident angles. Our experience showed that this type of approximation can be problematic for the quantitative interpretation of results. Previous studies also did not consider true surface optical effects. Lanni et al. (1985) corrected the experimen-

tal data assuming a distance-dependent collecting efficiency based on the work of Lukosz and Kunz (1977). This approach assumes the fluorophore emission to be a fixed-amplitude dipole oscillation, yielding a variable-power dissipation. The dissipation of power of a fluorophore under steady illumination must equal the constant fluorophore input power, which is best described with a variable-amplitude dipole oscillator model for fluorophore emission. Hellen and Axelrod (1987) showed that this modified model (see Appendix) leads to distinctly different predictions for distance-dependent collection efficiency.

Based on the theoretical simulations and experimental measurements reported here, it appears that z-resolution of >10 nm is readily achievable for bright fluorophores and defined fluorophore geometries. A priori specification of the fluorophore distribution profile permits determination of distance parameters by nonlinear least-squares regression to an analytical form of the Laplace transform of the fluorophore distribution. It is noted that the z-resolution of MA-TIRFM can be improved by increasing the number of incident angles used for the parameter regression; however, extended data acquisition times and photobleaching limit the practicality of collecting data at >25 angles. Simulations indicated that the resolution can be improved, not only by increasing the number of angles, but also by optimizing the sampled angles for the expected fluorophore distribution (Fig. 3, A–C). Our impression is that recovery of fluorophore distributions of arbitrary functional form by direct inverse Laplace transform (e.g., by complex integration using the Heaviside expansion theorem; Boas, 1983) or by the maximum entropy method (Livesey and Brockon, 1987), is not practical at this time. An additional complexity in the recovery of an arbitrary distribution function would be correction for nonuniform collection efficiency.

Notwithstanding these caveats, the MA-TIRFM approach has a number of potential applications to biological problems in living cells where existing methods cannot be applied. The measurements here of cell-substrate contact confirmed the results from previous studies (see Results) and provided quantitative 3-d surface contact maps. The MA-TIRFM approach should be useful to measure skeleton-plasma membrane distances, such as the spatial distribution of the spectrin membrane skeleton in erythrocytes (McGough and Josephs, 1990; Winkelmann and Forget, 1993). TIRF has been applied recently to visualize agonist-induced exocytosis of intracellular granules after labeling by fluorescent weak bases (Steyer and Almers, 1997; Oheim et al., 1997). MA-TIRFM should permit the quantitative determination of membrane-granule distances, the correlation of distances with granule properties (such as pH and calcium), and the measurement of kinetics of granule movement to and fusion with the plasma membrane. Another potential application of MA-TIRFM is analysis of cell locomotion, where the topological changes that occur as cells crawl could be quantified.

APPENDIX

The theory developed by Hellen and Axelrod (1987) was adapted to compute the distance-dependent collection efficiency, $Q(z)$, introduced in Eq. 10. The equations presented below apply to the case of a fluorophore distribution with random dipole orientation, excited by s-polarized light. To avoid confusion it is noted that the symbol θ is here used to denote the azimuthal angle, not the incident angle as previously.

The system under investigation consists of a single interface between an aqueous layer containing the fluorophore (refractive index n_2) and a glass prism (n_1). The plane of origin ($z = 0$) is taken to be the interface, and z is positive in medium 2. The location and orientation of a dipole is given by $\mathbf{r}'(z, \phi', \theta')$, where z is the distance from the interface, and the azimuthal angle ϕ' and polar angle θ' define the orientation of the dipole. The observation point is specified by $\mathbf{r}(r, \phi, \theta)$, where r, ϕ, and θ are spherical coordinates. $S(\mathbf{r},\mathbf{r}')$ is the radiated emitted intensity from a fixed-amplitude dipole oscillator at $\mathbf{r}'$ observed at $\mathbf{r}$. As discussed in the Theory section, the fluorophore is modeled as a fixed power and variable amplitude dipole. The intensity $S(\mathbf{r},\mathbf{r}')$ is thus divided by the total power dissipated by the fixed amplitude dipole, $P_T(\mathbf{r}')$, resulting in the radiated intensity per unit of absorbed power $\bar{S}(\mathbf{r},\mathbf{r}') = S(\mathbf{r},\mathbf{r}')/P_T(\mathbf{r}')$. The product of $\bar{S}$ and the excitation intensity, I_{ex} (in the case of evanescent wave excitation I_{ex} is given by Eq. 1), gives the intensity radiated from a fixed power dipole: $I(\mathbf{r},\mathbf{r}') = I_{ex}(z) \bar{S}(\mathbf{r},\mathbf{r}')$. For a fluorophore distribution, $D(z)$, with random dipole orientation, the intensity observed at $\mathbf{r}$ is:

$$\mathcal{I}(\mathbf{r}) = k \int_0^\infty \int_0^\pi \int_0^{2\pi} I(\mathbf{r},\mathbf{r}')D(z) \sin \theta' d\phi' d\theta' dz \quad \text{(A1)}$$

where k is a proportionality constant. The total fluorescence collected by a microscope objective, $\mathcal{F}$, at a distance r, is the integral of $\mathcal{I}(\mathbf{r})$ over the objective's aperture:

$$\mathcal{F}(\mathbf{r}) = \int_0^{\theta_{max}} \int_0^{2\pi} r^2 \mathcal{I}(\mathbf{r}) \sin \theta \, d\phi \, d\theta \quad \text{(A2)}$$

where $\theta_{max} = \arcsin(NA/n_2)$ is the polar observation angle, and NA is the numerical aperture of the objective.

Using the above equations, the collection efficiency $Q(z)$, as defined in Eq. 10, can be expressed in terms of single integrals. The equations to calculate $Q(z)$ for the special case here (single dielectric interface, s-polarized excitation light, observation through the aqueous medium) are given. For a rigorous derivation of the general expression for $Q(z)$, see Hellen and Axelrod (1987).

$Q(z)$ can be expressed as the weighted linear combination of the collection efficiencies for dipoles oriented parallel, $Q^\|(z)$, and perpendicular, $Q^\perp(z)$, to the interface:

$$Q(z) = [w^\| Q^\|(z) + w^\perp Q^\perp(z)]/(w^\| + w^\perp) \quad \text{(A3)}$$

where the weighting factors are:

$$w^\| = \int_0^\pi \frac{\sin^5 \theta' d\theta'}{\sin^2 \theta' + [\eta(z)]^{-1} \cos^2 \theta'}$$

$$\text{(A4)}$$

$$w^\perp = \int_0^\pi \frac{\sin^3 \theta' \cos^2 \theta' d\theta}{\cos^2 \theta' + [\eta(z)] \sin^2 \theta'}$$

and $\eta(z) = P_T^\|(z)/P_T^\perp(z)$, where $P_T^{\|,\perp}(z)$ are the total powers dissipated by fixed-amplitude dipoles oriented parallel and perpendicular to the interface.

$$P_T^\|(z) = [c\mu^2 k_2^4/4n_2^3] \, \text{Re}\left[\int_0^\infty \nu(1 - \nu^2)^{-1/2}\right.$$
$$\cdot \{(1 + r^s \exp(i2k_2z(1 - \nu^2)^{1/2})) + ((1 - \nu^2) \quad \text{(A5)}$$
$$\left. \cdot (1 - r^p \exp(i2k_2z(1 - \nu^2)^{1/2}))\} \, d\nu\right]$$

$$P_T^\perp(z) = [c\mu^2 k_2^4/2n_2^3]$$
$$\text{Re}\left[\int_0^\infty \nu^3(1 - \nu^2)^{-1/2}(1 + r^p \exp(i2k_2z(1 - \nu^2)^{1/2})) \, d\nu\right]$$
$$\text{(A6)}$$

where c is the speed of light in vacuum, $k_2 = 2\pi n_2/\lambda$, and μ is the dipole moment. The integration variable, ν, is the sine of the polar angle of the emitted light and goes from zero to infinity to account for the complex wavenumbers corresponding to the near field of the dipole. r^p and r^s are the reflection coefficients for p and s-polarized light respectively, and can be expressed as a function of ν:

$$r^p = \frac{(1 - \nu^2)^{1/2} - \epsilon_{21}(\epsilon_{12} - \nu^2)^{1/2}}{(1 - \nu^2)^{1/2} + \epsilon_{21}(\epsilon_{12} - \nu^2)^{1/2}} \quad \text{(A7)}$$

$$r^s = \frac{(1 - \nu^2)^{1/2} - (\epsilon_{12} - \nu^2)^{1/2}}{(1 - \nu^2)^{1/2} + (\epsilon_{12} - \nu^2)^{1/2}} \quad \text{(A8)}$$

where $\epsilon_{12} = (n_1/n_2)^2$, and $\epsilon_{21} = (n_2/n_1)^2$. The parallel and perpendicular collection efficiencies are:

$$Q^{\|,\perp}(z) = 2\pi r^2 \int_0^{\theta_1} \langle \bar{S} \rangle_\phi^{\|,\perp}(z, \theta) \sin \theta \, d\theta \quad \text{(A9)}$$

where $\langle \bar{S} \rangle_\phi^{\|,\perp}$ are the ϕ-averaged and normalized intensities radiated by dipoles parallel and perpendicular to the interface:

$$\langle \bar{S} \rangle_\phi^\|(z, \theta) = cn_2(|E^p|^2 + |E^s|^2)/16\pi P_T^\|(z);$$
$$\langle \bar{S} \rangle_\phi^\perp(z, \theta) = cn_2|E^z|^2/8\pi P_T^\perp(z)$$
$$\text{(A10)}$$

where E^p, E^s, and E^z are electric fields produced by dipoles oriented along the directions p, s, and z at a distance z from the interface and observed at a point defined by r and θ. p and s are parallel to the interface, with p being parallel to and s perpendicular to the plane of observation. z is the along the z-axis. In the aqueous medium the electric field intensities are:

$$|E^p|^2 = [\mu^2 k_2^4/n_2^4 r^2]\cos^2 \theta \, |\exp(-i2k_2z \cos \theta) - r^p|^2 \quad \text{(A11)}$$

$$|E^s|^2 = [\mu^2 k_2^4/n_2^4 r^2] \, |\exp(-i2k_2z \cos \theta) + r^s|^2 \quad \text{(A12)}$$

$$|E^z|^2 = [\mu^2 k_2^4/n_2^4 r^2]\sin^2 \theta \, |\exp(-i2k_2z \cos \theta) + r^p|^2 \quad \text{(A13)}$$

The collection efficiency, $Q(z)$, was computed by numerical integration of Eqs. A4, A5, A6, and A9. For the improper integrals (A5 and A6), the extended midpoint rule was used, while the closed integrals were computed with the extended trapezoidal rule. The program to compute $Q(z)$ for specified n_1, n_2, NA, and λ was written in C and is available upon request.

REFERENCES

Abercrombie, M., J. E. M. Heaysman, and S. M. Pegrum. 1971. The locomotion of fibroblasts in culture. IV. Electron microscopy of the leading lamella. *Exp. Cell. Res.* 67:359–367.

Axelrod, D. 1981. Cell-substrate contacts illuminated by total internal reflection fluorescence. *J. Cell Biol.* 89:141–145.

Axelrod, D., T. P. Burghardt, and N. L. Thompson. 1984. Total internal reflection fluorescence. *Ann. Rev. Biophys. Bioeng.* 13:247–268.

Bicknese, S., N. Periasamy, S. B. Shohet, and A. S. Verkman. 1993. Cytoplasmic viscosity near the cell plasma membrane: measurement by evanescent field frequency-domain microfluorimetry. *Biophys. J.* 65: 1272–1282.

Boas, M. L. 1983. Mathematical Methods in the Physical Sciences. 2nd Ed. John Wiley & Sons, New York.

Burghardt, T. P., and N. L. Thompson. 1984. Effect of planar dielectric interfaces on fluorescence emission and detection: evanescent excitation with high-aperture collection. *Biophys. J.* 46:729–737.

Burmeister, J. S., G. A. Truskey, and W. M. Reichert. 1994. Quantitative analysis of variable-angle total internal reflection fluorescence microscopy (VA-TIRFM) of cell-substrate contacts. *J. Microsc.* 173:39–51.

Burridge, K., K. Fath, T. Kelly, G. Nuckolls, and C. Turner. 1988. Focal adhesions: transmembrane junctions between the extracellular matrix and the cytoskeleton. *Annu. Rev. Cell. Biol.* 95:487–525.

Chen, W. T., and S. J. Singer. 1982. Immunoelectron microscopic studies of the sites of cell-substratum and cell-cell contacts in cultured fibroblasts. *J. Cell Biol.* 95:205–222.

Farinas, J., V. Simenak, and A. S. Verkman. 1995. Cell volume measured in adherent cells by total internal reflection microfluorimetry: application to permeability in cells transfected with water channel homologs. *Biophys. J.* 68:1613–1620.

Gingell, D., O. S. Heavens, and J. S. Mellor. 1987. General electromagnetic theory of total internal reflection fluorescence: the quantitative basis for mapping cell-substratum topography. *J. Cell Sci.* 87:677–693.

Gingell, D., I. Todd, and J. Bailey. 1985. Topography of cell-glass apposition revealed by total internal reflection fluorescence of volume markers. *J. Cell Biol.* 100:1334–1338.

Heaysman, J. E. M., and S. M. Pegrum. 1973. Early contacts between fibroblasts. An ultrastructural study. *Exp. Cell. Res.* 78:71–78.

Hellen, E. H., and D. Axelrod. 1987. Fluorescence emission at dielectric and metal-film interfaces. *J. Opt. Soc. Am. B.* 4:337–350.

Hsieh, H. V., and N. L. Thompson. 1994. Theory for measuring bivalent surface binding kinetics using total internal reflection with fluorescence photobleaching recovery. *Biophys. J.* 66:898–911.

Hsieh, H. V., and N. L. Thompson. 1995. Dissociation kinetics between a mouse Fc receptor and IgG—measurement by total internal reflection with fluorescence photobleaching recovery. *Biochemistry.* 34: 12481–12488.

Izzard, C. S., and L. R. Lochner. 1976. Cell-to-substrate contacts in living fibroblasts: an interference reflection study with an evaluation of the technique. *J. Cell Sci.* 21:129–159.

Lanni, F., A. S. Waggoner, and D. L. Taylor. 1985. Structural organization of interphase 3T3 fibroblasts studied by total internal reflection fluorescence microscopy. *J. Cell Biol.* 100:1091–1102.

Lee, E., R. E. Benner, J. B. Fenn, and R. K. Chang. 1979. Angular distribution of fluorescence from liquids and monodispersed spheres by evanescent wave excitation. *Appl. Optics.* 18:862–868.

Livesey, A. K., and J. C. Brockon. 1987. Analyzing the distribution of decay constants in pulse-fluorimetry using the Maximum Entropy Method. *Biophys. J.* 52:693–706.

Lukosz, W., and R. E. Kunz. 1977. Light emission by magnetic and electric dipoles to a plane interface. I. Total radiated power. *J. Opt. Soc. Am.* 67:1607–1614.

McGough, A. M., and R. Josephs. 1990. On the structure of erythrocyte spectrin in partially expanded membrane skeletons. *Proc. Natl. Acad. Sci. USA.* 87:5208–5212.

Oheim, M., R. H. Chow, and W. Stuhmer. 1997. Total internal reflection fluorescence microscopy (TIRFM) visualizes dynamics of secretory vesicles between distinct pools in bovine adrenal chromaffin cells. *Biophys. J.* 72:215a (Abstr.).

Pratt, W. K. 1991. Digital Image Processing. Wiley Interscience, New York.

Press, W. H., S. A. Teulkolsky, W. T. Vellering, and B. P. Flannery. 1992. Numerical Recipes in C. Cambridge University Press.

Reichert, W. M., P. A. Suci, J. T. Ives, and J. D. Andrade. 1987. Evanescent detection of adsorbed protein concentration distance profiles: fit of simple models to variable angle total internal reflection fluorescence data. *Appl. Spectrosc.* 41:503–508.

Reichert, W. M., and G. A. Truskey. 1990. Total internal reflection fluorescence (TIRF) microscopy. I. Modelling cell contact region fluorescence. *J. Cell Sci.* 96:219–230.

Rondalez, F., D. Ausserre, and H. Hervet. 1987. Experimental studies of polymer concentration profiles at solid-liquid and liquid-gas interfaces by optical and x-ray evanescent wave techniques. *Annu. Rev. Phys. Chem.* 38:317–347.

Steyer, J. A., H. Horstmann, and W. Almers. 1997. Transport, docking and exocytosis of single secretory granules in live chromaffin cells. *Nature.* 388:474–478.

Stout, A. L., and D. Axelrod. 1994. Reversible binding kinetics of a cytoskeletal protein at the erythrocyte submembrane. *Biophys. J.* 67: 1324–1334.

Suci, P. A., and W. M. Reichert. 1988. Determination of fluorescence density profiles of Langmuir-Blodgett-deposited films by analysis of variable-angle fluorescence data curves. *Langmuir.* 4:1131–1141.

Swaminathan, R., N. Periasamy, S. Bicknese, and A. S. Verkman. 1996. Cytoplasmic viscosity near the cell plasma membrane: translation of BCECF measured by total internal reflection-fluorescence photobleaching recovery. *Biophys. J.* 71:1140–1151.

Thompson, N. L., A. W. Drake, L. X. Chen, and W. VandenBroek. 1997. Equilibrium, kinetics, diffusion and self-association of proteins at membrane surfaces: measurement by total internal reflection fluorescence microscopy. *Photochem. Photobiol.* 97:39–46.

Truskey, G. A., J. S. Burmeister, E. Grapa, and W. M. Reichert. 1992. Total internal reflection fluorescence microscopy (TIRFM). II. Topographical mapping of relative cell/substratum separation distances. *J. Cell Sci.* 103:491–499.

Winkelmann, J. C., and B. C. Forget. 1993. Erythroid and nonerythrocyte spectrins. *Blood.* 81:3173–3185.